Nano Energy 78 (2020) 105397

Contents lists available at ScienceDirect

Nano Energy

journal homepage: http://www.elsevier.com/locate/nanoen

Wireless portable light-weight self-charging power packs by perovskite-organic tandem solar cells integrated with solid-state asymmetric supercapacitors

Tao Zhu [1], Yongrui Yang [1], Yanghe Liu, Raymond Lopez-Hallman, Zhihao Ma, Lei Liu, Xiong Gong [*]

School of Polymer Science and Polymer Engineering, College of Engineering and Polymer Science, The University of Akron, Akron, OH, 44325, USA

ARTICLE INFO

Keywords:
Wireless portable light-weight self-charging power packs
Integrated electric circuit
Tandem solar cells
Solid-state asymmetric supercapacitors
Solution-processed intermediate layers

ABSTRACT

Self-charging power packs possess great potential applications in the micro-systems, but these electric circuits are required to be portable, light-weight and even wireless connected for practical applications, in particular, in the wearable and portable electronics. In this study, we report wireless portable light-weight solution-processed self-charging power packs by tandem solar cells integrated with solid-state asymmetric supercapacitors through solution-processed electrical conductive polymeric thin film. Towards the end, we first develop solution-processed tandem solar cells by perovskite solar cells (PSCs) combined with ternary organic solar cells (OSCs) for achieving large operational voltage. We then develop solid-state asymmetric supercapacitors by both novel positive electrode and solid-state polymeric electrolytes for enhancing the energy density and cycling stability. After that, we integrate PSCs–OSCs tandem solar cells with solid-state asymmetric supercapacitors through solution-processed electrical conductive polymeric thin film to build wireless portable light-weight solution-processed self-charging power packs. This novel self-charging power packs not only possess advanced features such as portable, light-weight and wireless connection, but also exhibit excellent electric-circuit device performance, such as with an overall efficiency of 12.43% and an energy storage efficiency of 72.4% under white light illumination. All these results demonstrate that the wireless portable light-weight self-charging power packs through utilization of tandem solar cells as the renewable energy source and solid-state asymmetric supercapacitors as the energy storage device connected with solution-processed electrical conductive polymeric thin film, for the first time, are developed.

1. Introduction

Self-charging power packs are a new type of electronics that operated by the stored energy, which was generated by multifarious forms of energy such as light, sound and heat [1]. With this new technology for uninterrupted power supply, one can greatly extend the lifetime of electronics. The self-charging power packs are of importance in the new generation of micro-systems including remote sensors, implantable biosensors and nano-robots [2–5]. However, current self-charging power packs constrain the system performance and do not meet customers' satisfaction [6]. The self-charging power packs driven by supercapacitors incorporated with liquid electrolytes, which were charged by solar cells have been reported by us and others a few years ago [7–11]. For example, Peng et al. [9] developed flexible energy fiber by integrating polymer solar cells with supercapacitors, which exhibited superior flexibility but a lower overall efficiency of 0.82%. Recently, perovskite/silicon tandem solar cells and redox flow batteries based on bis-(trimethylammonio)propylbviologen (BTMAP-Vi) and 4-trimethylammonium-TEMPO (NMe-TEMPO) redox couples to realize high-performance and stable solar flow battery device was reported [11]. But tandem solar cells based on perovskite/silicon not only required cost-expensive manufacturing processes, but also restricted its compatibility with flexible and lightweight applications [11]. In addition, the self-charging power packs were fabricated through metal wires to connect two different electronic devices restricted its practical applications, in particular, in wearable and portable electronics [7–10].

* Corresponding author.
E-mail address: xgong@uakron.edu (X. Gong).
[1] These authors are equally contributed to this work.

https://doi.org/10.1016/j.nanoen.2020.105397
Received 1 August 2020; Received in revised form 9 September 2020; Accepted 14 September 2020
Available online 17 September 2020

Thus, the wireless self-charging power packs based on all-solution processed solar cells and solid-state supercapacitors need to be developed.

As solar cell technology, organic solar cells (OSCs) and perovskite solar cells (PSCs) have been attracted great attention in both academic and industrial sectors due to their light-weight and cost-effective manufacturing processes [12–16]. Single junction PSCs with over 25.2% power conversion efficiencies (PCEs) have been reported last year [13]. Single junction OSCs with over 18% PCEs were reported recently [12]. However, the open-circuit voltages (V_{OC}) observed from both single junction PSCs and OSCs were too small to be used for the operation of most electronics. In order to enlarge V_{OC} and thus PCEs, tandem solar cells have been developed [17,18]. In the past years, the overwhelming majority of developments in tandem solar cells has been focused on PSCs combined with either copper-indium-gallium-diselenide (CIGS) solar cells or silicon solar cells [19–22]. Tandem solar cells by PSCs with OSCs possess great advantages since both of them share the same device structures and can be fabricated by cost-effective solution processed method [12–16], However, the PSCs–OSCs tandem solar cells exhibited poor device performance as compared with either PSCs-CIGS or PSCs–Si tandem solar cells [19–22].

As an energy storage device, supercapacitors have been used in the self-charging power packs due to its fast charge and discharge times, high power density and excellent electrochemical stability [7–11,23,24]. The supercapacitors for fabrication of self-charging power packs were incorporated with liquid electrolytes and exhibited low energy density [7–10], which limit its practical applications [25–28]. Towards the end, supercapacitors incorporated with non-toxic solid-state electrolytes that exhibit high energy densities need to be developed for practical applications [25–28].

To boost energy density of supercapacitors, pseudocapacitive electrodes and asymmetric device structure have been developed [29,30]. Compared to both transition metal oxides and transition metal sulfides, transition metal selenides possess higher electrical conductivities, which make them as potential materials for the positive electrodes in supercapacitors [31–33]. Polyaniline (PANI) was widely developed pseudocapacitive material since it provided large pseudocapacitance and good flexibility [34,35]. PANI mixed with $MnSe_2$ nanoparticles not only provide good flexibility, but also prevent the aggregate of $MnSe_2$ nanoparticles. Therefore the PANI:$MnSe_2$ composites as the positive electrodes are expected to have both high pseudocapacitance and good flexibility. Reduced graphene oxides are chosen as the negative electrode owing to its high electrical conductivity, large surface area, good mechanical flexibility and excellent stability in various electrolytes [36–38].

In this study, we first report the development of solution-processed tandem solar cells fabricated by PSCs combined with ternary OSCs. PSCs–OSCs tandem solar cells exhibit a V_{OC} of 1.64 V and a PCE of 17.16%, which are among the best device performance parameters from PSCs–OSCs tandem solar cells. We then report the development of solid-state asymmetric supercapacitors (ASCs) by both novel positive electrode and solid-state polymeric electrolytes. The solid-state ASCs exhibit an operational voltage of 1.60 V, an energy density of 42.1 Wh/kg and a cycling stability of 2000 cycles. Afterward, for the first time, we report the development of solution-processed self-charging power packs by PSCs–OSCs tandem solar cells integrated with solid-state ASCs through solution-processed electrical conductive polymeric thin film. The self-charging power packs not only possess portable, light-weight and wireless connection advanced features, but also exhibit outstanding electric-circuit device performance such as with an overall efficiency of 12.43% and an energy storage efficiency of 72.4% under white light illumination.

2. Materials and methods

2.1. Materials

Poly[[4,8-bis[(5-ethylhexyl)thienyl]benzo [1,2-b,3,3-b]dithiophene-2,6-diyl][3-fluoro-2-[(2-ethylhexyl) carbonyl] thieno [3,4-b] thiophenediyl]] (PTB7-DT) [6,6],-phenyl-C71-butyric acid methyl ester ($PC_{71}BM$) were purchased from 1-Materials Inc. O6T-4F (also known as COi8DFIC), was provided by Prof. Liming Ding's group [39]. Poly[9,9-bis (6′-(N,N-diethylamino)propyl)-fluorene-alt-9,9-bis-(3-ethyl(oxetane-3-ethyloxy)-hexyl)-fluorene] (PFN-OX) is synthesized based on the method reported in our previous work [40]. Polyethylene oxide (PEO) (with molecular weight (Mw) of 500 g/mol) was purchased from Scientific Polymer Inc. Tin oxide (15% colloidal dispersion in water) and tin oxide nanoparticle ink in butanol, and lead iodide (PbI_2, 99.9985% metals basis) were purchased from Alfa Aesar. 2,2′,7,7′-tetrakis[N,N-di(4-methoxyphenyl) amino]-9,9′-spirobifluorene (spiro-OMeTAD) (99%), tert-butylpyridine (98%), bis(trifluoromethane)sulfonimide lithium salt (LiTFSI) (99.95%), tetrabutyl titanate (TBT), acetonitrile (ACN, anhydrous, 99.8%), poly (sodium 4-styrenesulfonate) (PSS) solution, dimethylformamide (DMF, anhydrous, 99.8%), zinc acetate (99.99% trace metals basis), ethanolamine (≫98%), chlorobenzene (CB) and 2-methoxyethanol (anhydrous, 99.8%) were purchased from Sigma-Aldrich. Methylammonium iodide (MAI, CH_3NH_3I) was purchased from Greatcell Solar. All materials were used as received without further processing.

2.2. Preparation and characterization of thin films

The ZnO precursor solution was prepared by dissolving both of zinc acetate and ethanolamine in 2-methoxyethanol at a concentration of 0.5 mol L^{-1} [41]. ZnO thin film (~40 nm) was spin-casted on the top of pre-cleaned ITO (indium tin oxides) glass from ZnO precursor solution, followed with thermal annealing at 200 °C for 60 min (min). Afterward, ZnO thin film was ultrasonicated in isopropyl alcohol and subsequently dried in an oven for further use.

TiO_X precursor solution (1 M) was prepared by diluting TBT with isopropyl alcohol solution (concentration of 3 vol%). The resultant solution was magnetically stirred for over 12 h (h) for further use.

The modified PEDOT:PSS (M-PEDOT:PSS) was made by mixing PEDOT:PSS solution (SCA 388-20) with PSS solution (15 mg/mL in H_2O) [42]. The volume ratio for this study is PEDOT:PSS:PSS = 1:1.5. The resultant solutions were magnetically stirred for over 12 h for further applications. The PEO-doped PEDOT:PSS solution was prepared by mixing PEDOT:PSS solution with 0.8 vol% of PEO [43]. The resultant solution was magnetically stirred for over 12 h for further use.

The PTB7-DT:O6T-4F:$PC_{71}BM$ bulk heterojunction (BHJ) thin film was solution-deposited on the top of the pre-cleaned substrates from 10 mg/mL CB solution, at 1500 rpm for 35 s (s).

The $CH_3NH_3PbI_3$ precursor solution (1.2 M) was prepared by mixing PbI_2 with MAI (1:1, molar ratio) in a mixed solvent of DMF with DMSO (4:1, volume ratio). The solution was spin-coated on the pre-cleaned substrates at 4000 rpm for 35 s. About 100 μL of toluene was poured on the thin film at 20 s to control the crystallization $CH_3NH_3PbI_3$ thin film. After that, $CH_3NH_3PbI_3$ thin films were post annealed at 100 °C for 10 min.

The absorption spectra of PTB7-DT:O6T-4F:$PC_{71}BM$ BHJ thin film and $CH_3NH_3PbI_3$ thin film were characterized with a Lambda 900 UV–vis–NIR spectrophotometer (PerkinElmer, Waltham, MA, USA). The field-emission scanning electron microscope (JEOL-7401) was applied to obtain the cross-section scanning electron microscopy (SEM) images.

2.3. Fabrication and characterization of tandem solar cells

Fabrication of tandem solar cells: Tandem solar cells were fabricated with a device architecture of ITO/ZnO/PTB7-DT:$PC_{71}BM$:O6T-4F/intermediate layers/$CH_3NH_3PbI_3$/spiro-OMeTAD/Ag, where Ag is sliver. The organic active layer, the PTB7-DT:$PC_{71}BM$:O6T-4F BHJ composite layer, was fabricated via the process described in the fabrication of ternary OSCs (Supporting Information 1 (SI 1)), but without Al electrode, where Al is aluminum. The optimization of the intermediate layers in details is described in SI 2. Subsequently, M-PEDOT:PSS (or

PEO-doped PEDOT:PSS) was spin-coated on the top of the PTB7-DT:$PC_{71}BM$:O6T-4F BHJ composite layer, followed with thermal annealing at 105 °C for 10 min in the glovebox with nitrogen atmosphere. Then SnO_2 (or TiO_x) thin film was spin-coated on the top of M-PEDOT:PSS layer from SnO_2 solution, followed with thermal annealing at 105 °C for 10 min in the glovebox with nitrogen atmosphere. The PFN-OX thin layer was then spin-coated on the top of SnO_2 layer (or TiO_x layer) from PFN-OX methanol solution, followed with thermal annealed at 105 °C for 5 min in the glovebox with nitrogen atmosphere. Afterward, $CH_3NH_3PbI_3$ with was deposited from the precursor solution by one-step method as described in the fabrication of PSCs (SI 1). ~ 100 μL of toluene was poured on the top of $CH_3NH_3PbI_3$ thin film for 20 s to control the crystallization of $CH_3NH_3PbI_3$ thin film, followed with post-annealing at 100 °C for 10 min. After that, ~80 nm spiro-OMeTAD thin film was deposited on the top of $CH_3NH_3PbI_3$ thin film using the method described in the fabrication of PSCs (**SI 1**). Finally, ~100 nm Ag was successively evaporated on the top of spiro-OMeTAD layer in the vacuum system with a pressure of 6×10^{-6} Pa. The effective device area was measured to be 0.045 cm^2.

Characterizations of tandem solar cells: The current densities versus voltages (J-V) characteristics were obtained from a Keithley model 2400 source measurement. A Newport Air Mass 1.5 Global (AM1.5G) full-spectrum solar simulator was supplied as the light source. The external quantum efficiency (EQE) spectra of solar cells were performed using a solar cell quantum efficiency measurement system of European Solar Test Installation (ESTI). The transient photocurrent (TPC) measurement was performed through the home-made setup: [44].

2.4. Fabrication and characterization of the solid-state ASCs

Fabrication of the solid-state ASCs: The CC/PANI:$MnSe_2$//PVA:H_2SO_4//rGO/CC solid-state ASCs were fabricated by assembling the PANI:$MnSe_2$/CC electrode, where CC is carbon cloth, the rGO is reduced graphene oxide, which acts as negative electrode, and PVA:H_2SO_4 gel electrolyte into a sandwich-type cells construction (electrode/solid-state electrolyte/electrode). Finally, the cells were packaged using PET film.

Characterization of the solid-state ASCs: The cyclic voltammetry (CV) and galvanostatic charge and discharge (GCD) of the solid-state ASCs were performed by Gamry reference 3000 electrochemical workstations (Gamry Instruments, U.S.A). The cyclic stability was measured by LAND CT2001A (Landt Instruments, Wuhan China).

2.5. Fabrication and characterization of the wireless portable light-weight self-charging power packs

Fabrication of the wireless portable light-weight self-charging power packs: Tandem solar cells by ternary OSCs and PSCs are fabricated as described in the *2.3 Fabrication and characterization of tandem solar cells*. Afterward, a solution-processed electrical polymeric thin film, the FAI treated PEDOT:PSS thin film (where FAI is formamidinium iodide) was fabricated on the top of the Ag electrode of tandem solar cells [45,46]. Then the PANI:$MnSe_2$/CC electrode was attached on the top of the FAI treated PEDOT:PSS thin film. Finally, the solid-state ASCs are completed with the method described in *2.4 Fabrication and characterization of the solid-state ASCs*.

Characterization of the wireless portable light-weight self-charging power packs: A Newport Air Mass 1.5 Global (AM1.5G) full-spectrum solar simulator was supplied as the light source. The GCD data measurements were performed on Gamry reference 3000 electrochemical workstations (Gamry Instruments, U.S.A).

3. Results and discussion

Fig. 1a presents the molecular structures of PTB7-DT [47], $PC_{71}BM$ and O6T-4F (also known as CO_i8DFIC) [39,48]. The absorption spectra of PTB7-DT:$PC_{71}BM$:O6T-4F ternary BHJ composite thin film and $CH_3NH_3PbI_3$ thin film are presented in Fig. 1b. The absorption of $CH_3NH_3PbI_3$ thin film ranges from 300 nm to 780 nm, whereas the absorption of PTB7-DT:$PC_{71}BM$:O6T-4F ternary BHJ composite thin film ranges from 300 nm to 1100 nm. Thus, the combination of these two thin films covers spectral ranges from 300 nm to 1100 nm. Moreover, $CH_3NH_3PbI_3$ thin film could serve as a complementary absorber with respect to PTB7-DT:$PC_{71}BM$:O6T-4F ternary BHJ composite thin film. Thus, tandem solar cells through the integration of ternary OSCs fabricated by PTB7-DT:$PC_{71}BM$:O6T-4F ternary BHJ composite thin film, with PSCs fabricated by $CH_3NH_3PbI_3$ thin film could absorb light from 300 nm to 1100 nm, generating large short-circuit current (J_{SC}) and producing large V_{OC} as well if ternary OSCs and PSCs are connected in series.

The device configurations of ternary OSCs and PSCs are ITO/ZnO/PTB7-DT:$PC_{71}BM$:O6T-4F/intermediate layers, and intermediate layers/$CH_3NH_3PbI_3$/spiro-OMeTAD/Ag, respectively, where ITO is indium tin oxides and acts as the cathode, solution-processed ZnO acts as the electron extraction layer (EEL), spiro-OMeTAD acts as the hole extraction layer (HEL), and Ag is sliver and acts as the anode, respectively. Solution-processed PTB7-DT:$PC_{71}BM$:O6T-4F ternary BHJ composite thin film is used as the photoactive layer for ternary OSCs and solution-processed $CH_3NH_3PbI_3$ is used as the photoactive layer for PSCs, respectively. The fabrication and characterization of ternary OSCs and PSCs are described in SI 1. The intermediate layers act as the anode for ternary OSCs, but as the cathode for PSCs. Different solution-processed intermediate layers are investigated for the construction of tandem solar cells (SI 2). After optimization, the multilayers composing of M-PEDOT:PSS/SnO_2/PFN-OX, is finally selected as the intermediate layers for construction of tandem solar cells. Scheme 1a schematically displays the device architecture of tandem solar cells, which is a combination of ternary OSCs with PSCs through solution-processed M-PEDOT:PSS/SnO_2/PFN-OX intermediate layers. Since $CH_3NH_3PbI_3$ photoactive layer possesses relatively high absorption coefficient [15,16,49] compared to PTB7-DT:$PC_{71}BM$:O6T-4F ternary BHJ composite photoactive layer, and the optimized thickness of PTB7-DT:$PC_{71}BM$:O6T-4F ternary BHJ composite photoactive layer is ~115 nm, which is thinner than that (~210 nm) of $CH_3NH_3PbI_3$ photoactive layer (SI 1). Ternary OSCs is placed as the top sub-cell to catch the photons as much as possible, while PSCs is placed as the bottom sub-cell to harvest the photons pass through PTB7-DT:$PC_{71}BM$:O6T-4F ternary BHJ composite thin film. Such construction could maximize the photons to be efficiently absorbed, generating high J_{SC} from tandem solar cells.

Scheme 1b displays the cross-section SEM image of tandem solar cells. It is worthy to mention that all layers are solution-processed from their corresponding solutions except for the ITO coated glass substrates and the Ag electrode. Obviously, PTB7-DT:$PC_{71}BM$:O6T-4F ternary BHJ composite thin film and $CH_3NH_3PbI_3$ thin film are connected through solution-processed M-PEDOT:PSS/SnO_2/PFN-OX intermediate layers. Moreover, both the ZnO EEL and the spiro-OMeTAD HEL are clearly presented in the cross-section SEM images. These results demonstrate that tandem solar cells by PSCs integrated with ternary OSCs through solution-processed M-PEDOT:PSS/SnO_2/PFN-OX intermediate layers could be cost-effectively fabricated.

Scheme 1c displays the lowest unoccupied molecular orbital (LUMO) and the highest occupied molecular orbital (HOMO) energy levels of ZnO, $PC_{71}BM$, O6T-4F, PTB7-DT, M-PEDOT:PSS, SnO_2, PFN-OX, $CH_3NH_3PbI_3$, spiro-OMeTAD, and the work functions of the ITO and Ag electrodes. The LUMO energy levels of PTB7-DT (- 3.66 eV), O6T-4F (- 3.88 eV) and $PC_{71}BM$ (- 4.00 eV) show a stepwise alignment, which is favorable for the separated electrons to be transported from the PTB7-DT electron donor to the O6T-4F electron acceptor and then to the $PC_{71}BM$ electron acceptor, resulting in enhanced J_{SC} for ternary OSCs [48]. A small HOMO offset between $CH_3NH_3PbI_3$ (- 5.45 eV) and the spiro-OMeTAD (- 5.20 eV) HEL could ensure the separated holes to be efficiently transported, resulting in a large V_{OC} for PSCs. Ternary OSCs are connected with PSCs through the M-PEDOT:PSS/SnO_2/PFN-OX

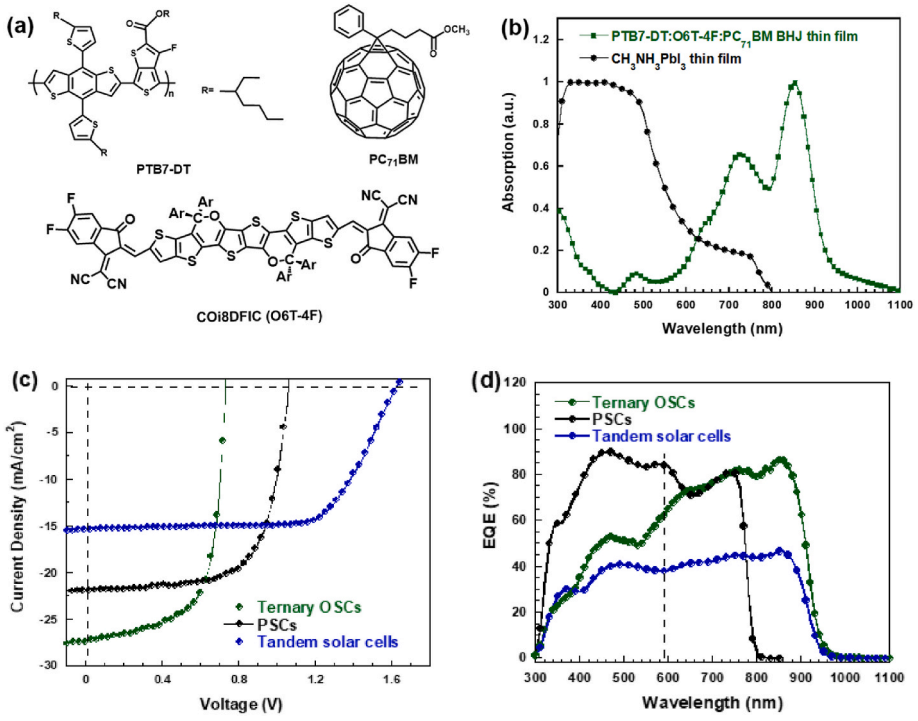

Fig. 1. (a) Molecular structures of PTB7-DT, O6T-4F, and $PC_{71}BM$, and (b) the absorption spectra of PTB7-DT:O6T-4F:$PC_{71}BM$ bulk heterojunction (BHJ) thin film and $CH_3NH_3PbI_3$ thin film. (c) The J-V characteristics and (d) the EQE spectra of ternary OSCs, PSCs and tandem solar cells.

intermediate layers. The M-PEDOT:PSS layer with a deep work function (- 5.00 eV) could collect the separated holes efficiently and sufficiently block the separated electrons to be transferred from PTB7-DT:$PC_{71}BM$: O6T-4F thin film to the SnO_2 EEL. A PFN-OX thin layer acts as the hole blocking layer and the EEL as well. The M-PEDOT:PSS/SnO_2/PFN-OX intermediate layers may boost the separated charge carriers to be efficiently transported, enhancing J_{SC} for tandem solar cells [40].

Fig. 1c presents the J-V characteristics of ternary OSCs, PSCs and tandem solar cells under white light illumination with a light intensity of 100 mW cm^{-2}. The device performance parameters of ternary OSCs, PSCs and tandem solar cells are summarized in SI 3. The ternary OSCs exhibit a J_{SC} of 27.21 mA/cm^2, a V_{OC} of 0.73 V, a fill factor (FF) of 65.8%, and with a corresponding PCE of 13.07%. These device performance parameters are in good agreement with reported values [39,48]. The PSCs exhibit a J_{SC} of 21.83 mA/cm^2, a V_{OC} of 1.07 V, an FF of 67.4%, and with a corresponding PCE of 15.68%. These device performance parameters are in good agreement with those reported values [50,51]. Tandem solar cells exhibit a J_{SC} of 15.32 mA/cm^2, a V_{OC} of 1.64 V, an FF of 68.3%, with the corresponding PCE of 17.16%. To the best of our knowledge, a PCE of 17.16% is the highest value to be reported from tandem solar cells constructed by PSCs with OSCs, so far [52–54]. Most importantly, a V_{OC} of 1.64 V obtained from tandem solar cells is close to the sum of V_{OC} values of ternary OSCs (0.73 V) and PSCs (1.07 V), which indicates that solution-processed tandem solar cells constructed by PSCs with ternary OSCs are successfully demonstrated. In addition, tandem solar cells exhibit minor changes in J_{SC} and V_{OC}, despite the triple enlargement of the device areas (Figs. S1 and SI 3).

The EQE spectra of ternary OSCs, PSCs and tandem solar cells are presented in Fig. 1c. The spectral response of tandem solar cells is a superimposed spectral response of PSCs and ternary OSCs, which further confirms the successful development of tandem solar cells. Based on the EQE spectra, the integrated current densities are calculated to be 22.96 mA/cm^2, 20.10 mA/cm^2 and 13.90 mA/cm^2 for ternary OSCs, PSCs and tandem solar cells, respectively. All these values are in good agreement with those from the J-V characteristics (Fig. 1d).

However, the observation of reduced EQE values from tandem solar cells compared to either ternary OSCs or PSCs is unfortunate, which indicates that both charge carrier generation and extraction in tandem solar cells are insufficient. In principle, a J_{SC} observed from tandem solar cells should be close to a smaller J_{SC} generated by either the top-cell or the bottom-cell [12–16]. In this study, PSCs generates a smaller J_{SC} compared to ternary OSCs. Thus, J_{SC} observed from tandem solar cells should be close to that from PSCs. However, a J_{SC} (15.32 mA/cm^2) observed from tandem solar cells is much smaller than that (21.83 mA/cm^2) from PSCs. In order to investigate the underlying physics of reduced J_{SC} from tandem solar cells, a TPC measurement is carried out to probe both charge carrier extraction times and photogenerated charge carrier densities in these solar cells [55,56]. With a monochromatic wavelength of 590 nm, the charge carrier extraction times of ~76, ~58, and ~93 ns (ns) are observed from ternary OSCs, PSCs and tandem solar cells, respectively (Fig. S2a, SI 3). Compared to both ternary OSCs and PSCs, a longer charge carrier extraction time observed from tandem solar cells confirms that the charge carrier extraction process is insufficient. Such longer charge carrier extraction time is probably attributed to the inevitable processes of charge carriers being trapped and de-trapped at the M-PEDOT:PSS/SnO_2/PFN-OX intermediate layer. The total extracted charge carrier densities from ternary OSCs, PSCs and tandem solar cells are further calculated by integration of the transient photocurrent density over the transient time [55,56] (Figs. S2b and SI 3). The extracted charge carrier densities for ternary OSCs, PSCs and tandem solar cells are 50.10 nC/cm^2, 64.77 nC/cm^2 and 31.34 nC/cm^2, respectively. Compared to tandem solar cells, more than 60% and 107% charge carriers are generated by ternary OSCs and PSCs, respectively; further indicating that the charge carrier extraction process is insufficient within tandem solar cells.

The steady-state light intensity-dependent V_{OC} and J_{SC} for ternary OSCs, PSCs, and tandem solar cells are further investigated to better understand the underlying device performance. The relations between V_{OC} and the light intensity is depicted as $V_{OC} \propto Sln(I)$, where $S = kT/q = 0.026$ (k is the Boltzmann's constant, T is the temperature, and q is the elementary charge at room temperature), and I is the light intensity [57, 58]. The fitted S values were 0.034, 0.032 and 0.046 for ternary OSCs,

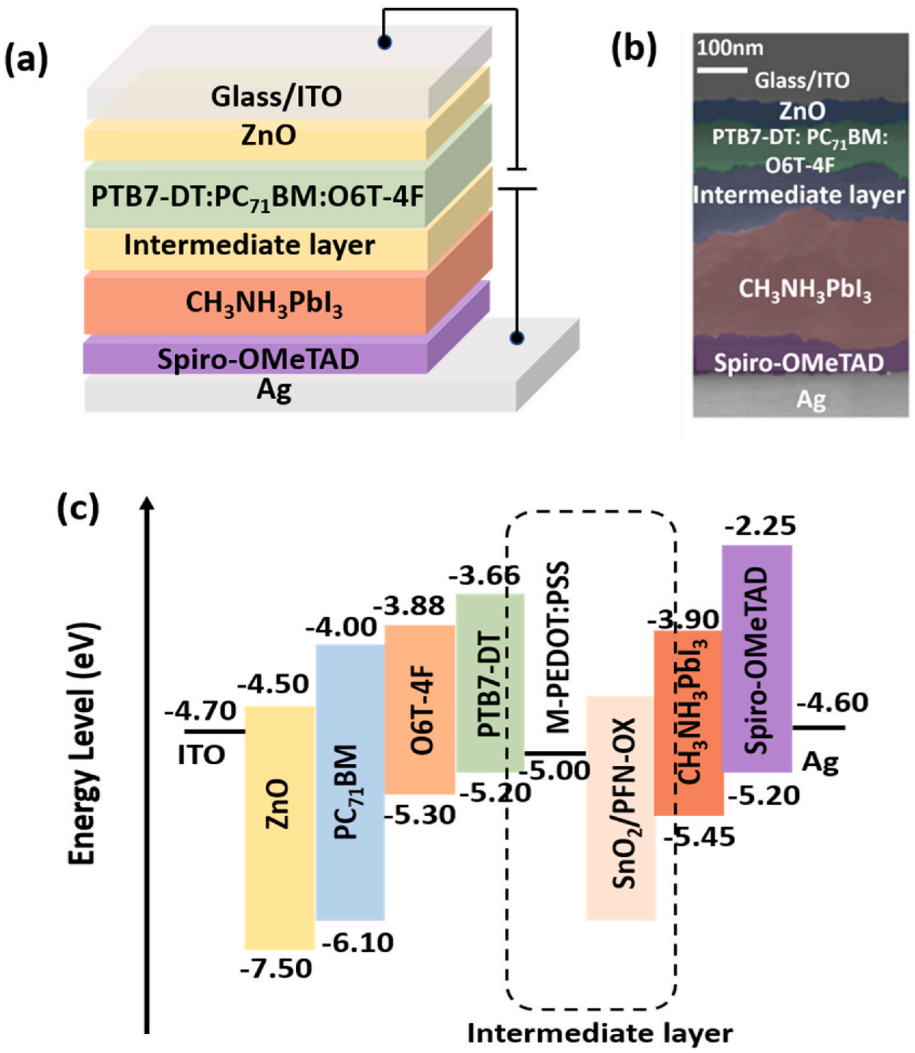

Scheme 1. (a) Schematic device structure and (b) the cross-sectional SEM images of tandem solar cells by ternary organic solar cells (OSCs) and perovskite solar cells (PSCs), (c) the LUMO and HOMO energy levels of ZnO, $PC_{71}BM$, O6T-4F, PTB7-DT, M-PEDOT:PSS, SnO_2, PFN-OX, $CH_3NH_3PbI_3$, spiro-OMeTAD, and the work functions of ITO and Ag electrodes, respectively.

PSCs and tandem solar cells, respectively (Figs. S3a and SI 3). A larger S observed from tandem solar cells indicates that the geminate recombination is responsible for small J_{SC}.

A near-linear dependence of J_{SC} with the light-intensity for ternary OSCs, PSCs, and tandem solar cells is observed (Figs. S3b and SI 3). J_{SC} dependence the light intensity (I) is described as $J_{SC} \propto I^{\alpha}$, where α is the coefficient. [57,58] α values of 0.94, 0.94 and 0.90 are observed from ternary OSCs, PSCs and tandem solar cells, respectively (Figs. S3b and SI 3). As α approximates to 1, which indicates that all charge carriers are swept out before recombination [57,58]. A smaller α observed from tandem solar cells indicates that the non-geminate recombination is dominated in tandem solar cells. As a result, a reduced J_{SC} is observed from tandem solar cells.

Theoretically, a V_{OC} from tandem solar cells should be a sum of V_{OC} values of ternary OSCs and PSCs, since ternary OSCs is connected in series with PSCs [12–16]. However, a V_{OC} of 1.64 V obtained from tandem solar cells is smaller than the sum of V_{OC} values (1.80 V) from ternary OSCs (0.73 V) and PSCs (1.07 V). Such voltage loss is attributed to poor electrical conductivity of the M-PEDOT:PSS/SnO_2/PFN-OX intermediate layers [19–22]. The SnO_2 EEL with PFN-OX interfacial layer can ensure ternary OSCs to be connected in series with PSCs and provide a strong dipole between the SnO_2 EEL and $CH_3NH_3PbI_3$ thin film, resulting in electron extraction from $CH_3NH_3PbI_3$ thin film. The SnO_2 EEL with a deep LUMO energy level inevitably restricts the separated electrons to be efficiently transported from $CH_3NH_3PbI_3$ thin film. Even though such electron transporting barrier is compromised by the dipole induced by the PFN-OX thin layer, the poor electrical conductivity of solution-processed SnO_2 EEL still impedes the separated electrons to be efficiently transported. As a result, a voltage loss occurs in tandem solar cells. But nevertheless, a V_{OC} observed from tandem solar cells is close to the sum of V_{OC} values of ternary OSCs and PSCs indicates that solution-processed tandem solar cells constructed by ternary OSCs with PSCs are successfully demonstrated. It should be noted that solution-processed tandem solar cells retains over 90% of its initial PCEs after 1800 s continuous illumination (Figs. S4 and SI 3), which implies that tandem solar cells possess relatively good stability, but tandem solar cells with workable stability certainly needs to be developed.

Solution-processed tandem solar cells exhibit a working voltage of 1.64 V, which is larger than 1.50 V, a typical voltage used for most commercial electronics. Thus, above solution-processed tandem solar cells are capable as a renewable energy source in self-charging power packs. Towards the end, we develop solid-sate ASCs. The following descriptions are the development of solid state ASCs.

It was reported that solid-state ASCs with rGO as the negative electrode exhibited high capacitance, which was ascribed to rGO's possessing large surface area, high electrical conductivity and abundant

open channels for ionic transporting [59,60]. Thus, rGO coated on the CC substrate is used as the negative electrode to enhance the flexibility of the rGO electrode since the CC substrate possesses excellent flexibility and good electrical conductivity [61]. The preparation of the rGO/CC negative electrode is described in SI 4.

As the positive electrode, on the other hand, the PANI mixed with $MnSe_2$ (PANI:$MnSe_2$) composites coated on the CC substrate is used, where PANI is polyaniline. Both large specific capacitance and good flexibility are expected to be observed from the PANI:$MnSe_2$/CC electrode since supercapacitors with either PANI or $MnSe_2$ as the positive electrodes exhibited superior specific capacitances [62,63]. The preparation and characterization of the PANI:$MnSe_2$/CC electrode are described in SI 5. Fig. 2a presents the CV of the PANI:$MnSe_2$/CC electrode. The CV curves of the PANI/CC and the $MnSe_2$/CC electrodes are also shown in Fig. 2a for comparison studies. As compared with both PANI/CC and $MnSe_2$/CC electrodes, the PANI:$MnSe_2$/CC electrode exhibits the largest CV curve area, which demonstrates that the PANI:$MnSe_2$/CC electrode possesses the largest specific capacitance. Interestingly, the CV curve area observed from the PANI:$MnSe_2$/CC electrode even larger than the sum of the $MnSe_2$/CC electrode and the PANI/CC electrode. Such enlarged CV area is suspected to be originated from poor electrical conductivity of $MnSe_2$ and poor stability of PANI [64].

The GCD curves of the PANI:$MnSe_2$/CC electrode, the PANI/CC and $MnSe_2$/CC electrodes are shown in Fig. 2b. The PANI:$MnSe_2$/CC electrode exhibits the longest discharge time compared to those from the PANI/CC and $MnSe_2$/CC electrodes. Based on the equations described in SI 6, the specific capacitances are calculated to be 850 F/g, 444 F/g, and 69 F/g for the PANI:$MnSe_2$/CC electrode, the $MnSe_2$/CC electrode and the PANI/CC electrode, respectively. These results further confirm that the PANI:$MnSe_2$/CC electrode possesses the largest specific capacitance compared to the PANI/CC and $MnSe_2$/CC electrodes.

Fig. 2c presents the CV curves of the PANI:$MnSe_2$/CC electrode scanned at the rates from 10 to 100 mV/s. Under different scan rates, the PANI:$MnSe_2$/CC electrode exhibits the same operational voltage window, from - 0.4 V to 0.8 V, and the shapes of CV curves don't show any significant change with the increase of scan rates. These results demonstrate that the PANI:$MnSe_2$/CC electrode has good reversible pseudocapacitive features [23]. Furthermore, the redox peaks are clearly observed from the CV curves of the PANI:$MnSe_2$/CC electrode even at high scan rates, which reveal that the PANI:$MnSe_2$/CC electrode possesses stable pseudocapacitive behaviors [23]. The kinetic evaluations are described in SI 6. The PANI:$MnSe_2$/CC electrode shows typical diffusion-controlled pseudocapacitance scanned from 10 to 100 mV/s (Figs. S9 and SI 5) [65–68].

Fig. 2d displays the specific capacitances of the PANI:$MnSe_2$/CC electrode under different current densities, where the specific capacitances are calculated based on the GCD curves as shown in insert of Fig. 2d. It is clearly that both charge and discharge curves are in good symmetry features from - 0.4 V to 0.8 V, which indicate that the PANI:$MnSe_2$/CC electrode possesses a great reversible electrochemical energy capacity behavior and fast charge-discharge property. Moreover, a couple of platforms presented in the charge-discharge curves indicate that typical redox reactions occurred in the PANI:$MnSe_2$/CC electrode, which is consistent with the electrochemical property as shown in their CV curves (Fig. 2c). The PANI:$MnSe_2$/CC electrode also shows a small series resistance of 2.94 Ω (SI 5), which indicates the PANI:$MnSe_2$/CC electrode has a high electrical conductivity [23]. As indicated in Fig. 2d, the PANI:$MnSe_2$/CC electrode remarkably possesses over 70% of its initial specific capacitance even under the current density of 10 A/g, which indicates that the PANI:$MnSe_2$/CC electrode exhibits a good rate capability [63]. Thus all these results clearly demonstrate that the PANI:$MnSe_2$/CC is a good positive electrode.

Fig. 3a schematically illustrates solid-state ASCs with a device configuration of CC/rGO//PVA:H_2SO_4//PANI:$MnSe_2$/CC, where PVA is polyvinyl alcohol. PVA:H_2SO_4 gel is used as the solid-state electrolytes since it possesses high ionic conductivity and excellent mechanical

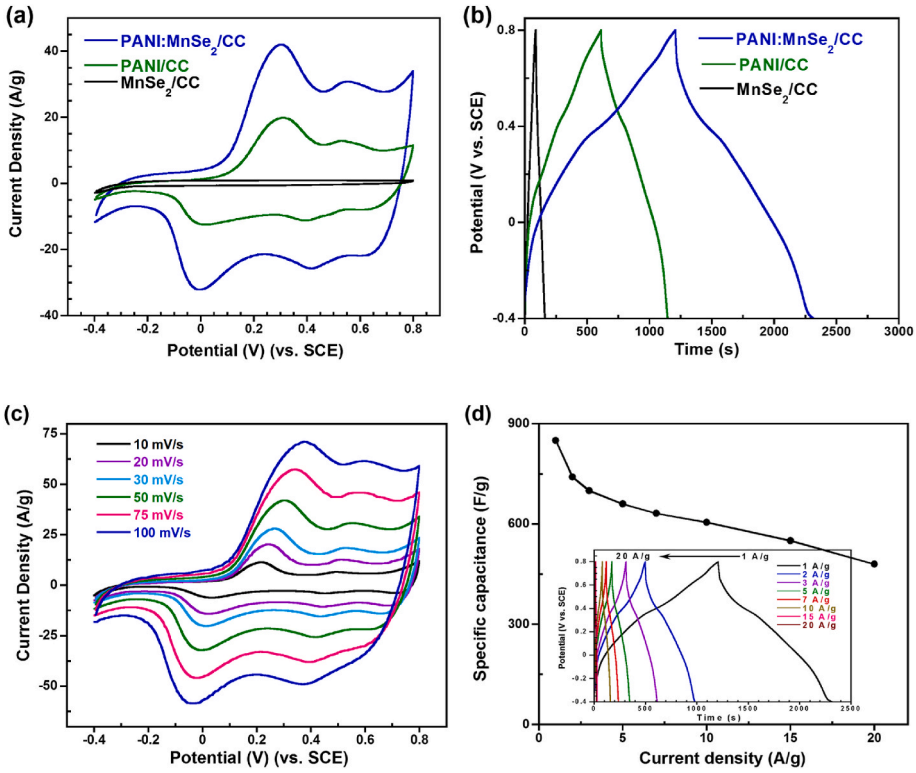

Fig. 2. (a) The cyclic voltammetry (CV) curves and (b) the galvanostatic charge and discharge (GCD) curves of the PANI:$MnSe_2$/CC, the PANI/CC and the $MnSe_2$/CC electrodes, (c) the CV curves of the PANI:$MnSe_2$/CC electrode scanned at different rates, and (d) the specific capacitances of the PANI:$MnSe_2$/CC electrode under different current densities, the insert of (d) are the GCD curves of the PANI:$MnSe_2$/CC electrode under different current densities.

flexibility [69,70], the rGO/CC and the PANI:$MnSe_2$/CC electrodes are used as the negative electrode and the positive electrode, respectively.

Fig. 3b displays the CV curves of solid-state ASCs scanned at different rates. The solid-state ASCs exhibit very similar CV shapes at the scan rates from 10 to 75 mV/s, which demonstrate that the PVA:H_2SO_4 solid-state gel electrolytes possess rapid ionic transporting, and further confirm that the rGO/CC electrode is matched very well with the PANI:$MnSe_2$/CC electrode [24,28]. Moreover, the solid-state ASCs exhibit a stable window of 1.60 V, indicating the solid-state ASCs possess a large operational voltage. In addition, a pair of peaks presented in the CV curves illustrate that the solid-state ASCs have typical reversible Faradic pseudocapacitive properties [28].

Fig. 3c presents the GCD curves of solid-state ASCs under different current densities. According to the equations described in SI 6, the specific capacitances are calculated. At the current density of 2 A/g, the solid-state ASCs exhibit a specific capacitance of 138 F/g (345 mF/cm^2). Even at the current density of 20 A/g, the solid-state ASCs still exhibit a specific capacitance of 52 F/g (130 mF/cm^2). These results demonstrate that the solid-state ASCs exhibit remarkable electrochemical stability at different current densities.

The energy densities versus power density (the Regone plot) of solid-state ASCs are shown in Fig. 3d. At the power density of 1500 W/kg, the solid-state ASCs exhibit an energy density of 41.7 Wh/kg. Even at the power density of 8000 W/kg, the solid-state ASCs exhibit an energy density of 22.0 Wh/kg. Such energy densities are better than those values from the solid-state ASCs by polyaniline-polyvinyl alcohol hydrogel (Ref. [1]) [71], or by β-MnO_2/birnessite (Ref. [2]) [72], or by $NiCo_2O_4$@MnO_2 (Ref. [3]) [73].

The insert of Fig. 3d is a cycling stability of solid-state ASCs. The solid-state ASCs maintain ~78% of its initial specific capacitance after 2000 cycles. However, a slightly reduction in the specific capacitance after 1500 cycles is observed. Such reduction is ascribed to the weak interaction between PANI and $MnSe_2$ within the PANI:$MnSe_2$ composite [64]. Overall, the results shown in Fig. 3d indicate that the solid-state ASCs possess large energy storage capacity and long-term electrochemical charge-discharge cycling stability.

All results shown in Fig. 3 demonstrate that the solid-state ASCs exhibit outstanding device performance parameters. The following descriptions are the development of wireless portable light-weight self-charging power packs integrated by PSCs–OSCs tandem solar cells with solid-state ASCs.

Fig. 4a schematically displays a device configuration of self-charging power packs. The self-charging power packs is integrated by tandem solar cells with solid-state ASCs through solution-processed electrical conductive polymeric thin film [45,46] rather than metal wires [7–10]. Similar to the metal wires, the electrical conductive polymeric thin film is used to facilitate the transportation of the generated photocurrent from tandem solar cells to the solid-state ASCs, resulting in the integration of solar energy generation and storage into one electrical circuit. Since both PSCs–OSCs tandem solar cells and solid-state ASCs developed in this study are portable and light-weight, and above two different devices are wireless connected through solution-processed electrical conductive polymeric thin film rather than metal wires, the self-charging power packs possess portable, light-weight and wireless connection advanced features.

Fig. 4b shows the discharge curve of wireless portable self-charging power packs charged by PSCs–OSCs tandem solar cell under white light illumination with the light intensity of 100 mW/cm^2. The discharge curve of wireless portable self-charging power packs charged by an electrochemical station at the current density of 2 mA/cm^2 is also shown in Fig. 4b for comparison study. It is clear that the discharge curves in both cases are similar, which demonstrates that the solid-state ASCs can be charged by solar energy generated by tandem solar cells. However, the voltage observed from solid-state ASCs charged by PSCs–OSCs tandem solar cells is 1.41 V, which is smaller than that (1.50 V) by an electrochemical station. But both of which are smaller than the operational window (1.60 V) observed from solid-state ASCs (Fig. 3b). These results illustrate that both tandem solar cells and an electrochemical station are unable to charge solid-state ASCs to its full operational voltage. Such voltage loss is probably due to poor electrical conductivity of solution-processed polymeric thin film [45,46]. More voltage loss observed from solid-state ASCs charged by tandem solar cells is probably ascribed to the reduced power output from tandem solar cells [10] and large contact resistance between solid-state ASCs and tandem solar cells

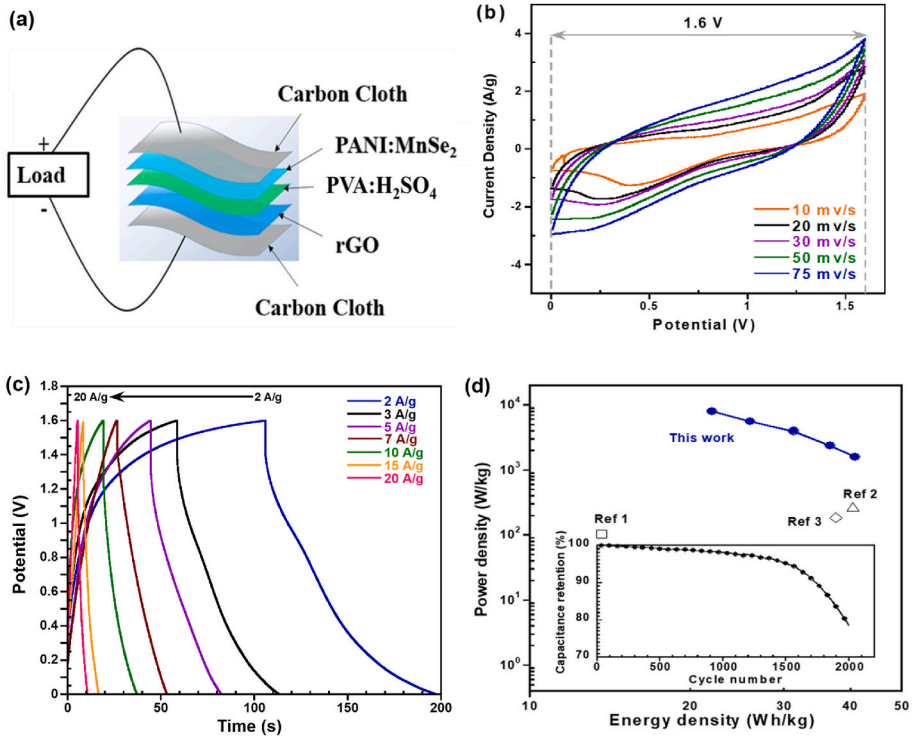

Fig. 3. (a) The schematic device structure of the solid-state asymmetric supercapacitors (ASCs), (b) the CV curves of the solid-state ASCs scanned at different rates, (c) the GCD curves of the solid-state ASCs under different current densities, and (d) the Ragone plot of the solid-state ASCs, where Ref [1] is the solid-state ASCs by polyaniline-polyvinyl alcohol hydrogel [71], Ref [2] is the solid-state ASCs by β-MnO_2/-birnessite [72], and Ref [3] is the solid-state ASCs by $NiCo_2O_4$@MnO_2 [73], respectively. The insert of (d) is the cycling stability of the solid-state ASCs.

[74,75].

Fig. 4c presents the discharge curves of solid-state ASCs in dark at the current densities from 1 mA/cm^2 to 20 mA/cm^2 after solid-state ASCs are charged by tandem solar cells. It is found that solid-state ASCs exhibit a specific capacitance of 234 mF/cm^2 at the current density of 1 mA/cm^2 (Fig. S12, SI 7). At the current density of 10 mA/cm^2, the specific capacitance is dropped to 100 mF/cm^2 (Figs. S12 and SI 7), which is, however, still a high capacitance as compared with those reported values [76,77]. These results demonstrate that the wireless portable light-weight self-charging power packs have a good energy capacity in a wide range of current densities.

The overall efficiency ($\eta_{overall}$) used for evaluating self-charging power packs is described as $\eta_{overall} = \frac{E_{SC}A_{SC}}{P_{light} \cdot S \cdot t_{charging}}$ [10], where E_{SC} is the energy density of supercapacitors, A_{SC} is the working area of supercapacitors, P_{light} is the light intensity of the standard AM 1.5G illumination (100 mW/cm^2), S is the working area of tandem solar cells, and $t_{charging}$ is the photo-charging time, respectively. The $\eta_{overall}$ for wireless portable light-weight self-charging power packs are shown in Fig. 4d. At the current density of 1 mA/cm^2, the wireless portable light-weight self-charging power packs exhibit a $\eta_{overall}$ of 12.43%, which is much higher than reported values [10,74,75]. Even at the current density of 10 mA/cm^2, the wireless portable light-weight self-charging power packs still possess a $\eta_{overall}$ of 5.36%. Such excellent device performance is attributed to both high PCE and large V_{OC} from tandem solar cells and high energy density from the solid-state ASCs.

The energy storage efficiency ($\eta_{storage}$) used for evaluating self-charging power packs is described as $\eta_{storage} = \eta_{overall}/\eta_{conversion}$ [10], where $\eta_{overall}$ is the overall efficiency of the self-charging power packs and $\eta_{conversion}$ is PCE of solar cells, respectively. Thus, a $\eta_{storage}$ of 72.4% is calculated for wireless portable light-weight self-charging power packs. Such high $\eta_{storage}$ indicates that tandem solar cells are matched with solid-state ASCs very well.

4. Conclusion

In summary, we reported wireless portable light-weight solution-processed self-charging power packs by tandem solar cells integrated with solid-state asymmetric supercapacitors through solution-processed electrical conductive polymeric thin film. Towards the end, we first reported solution-processed tandem solar cells by combination of PSCs with ternary OSCs. PSCs–OSCs tandem solar cells exhibited an open-circuit voltage of 1.64 V and a power conversion efficiency of 17.16%, which were one of the highest values from PSCs–OSCs tandem solar cells. Afterward, we reported solid-state asymmetric supercapacitors (ASCs) fabricated by both novel positive electrode and solid-state polymeric electrolytes. The solid-state ASCs exhibited outstanding device performance such as with an operational voltage of 1.60 V, an energy density of 42.1 Wh/kg and a cycling stability after 2000 cycles. Lastly, for the first time, to the best of our knowledge, we reported the development of solution-processed wireless portable light-weight self-charging power packs by tandem solar cells integrated with solid-state ASCs through solution-processed electrical conductive polymeric thin film. This novel self-charging power packs not only possessed advanced features such as portable, light-weight and wireless connection, but also exhibited excellent electric-circuit device performance, such as with an overall efficiency of 12.43% and an energy storage efficiency of 72.4% under white light illumination. All these results demonstrated that the wireless portable light-weight self-charging power packs were developed by utilization of tandem solar cells as the renewable energy sources integrated with solid-state asymmetric supercapacitors as the energy storage devices through solution-processed electrical conductive polymeric thin film.

Credit author statement

Tao Zhu: Methodology, investigation and data analysis on tandem solar and integrated device, Writing-original draft. **Yongrui Yang:** Methodology, investigation and data analysis on supercapacitor and integrated device, Discussion. **Yanghe Liu:** conducting all experiments suggested by the reviewers. **Raymond Lopez-Hallman**: Resources, Discussion. **Zhihao Ma:** Resources, Discussion. **Lei Liu:** Writing-Reviewing & Editing. **Xiong Gong:** Project administration, Funding acquisition, Writing-reviewing & Editing.

Declaration of competing interest

The authors declare that they have no known competing financial interests or personal relationships that could have appeared to influence

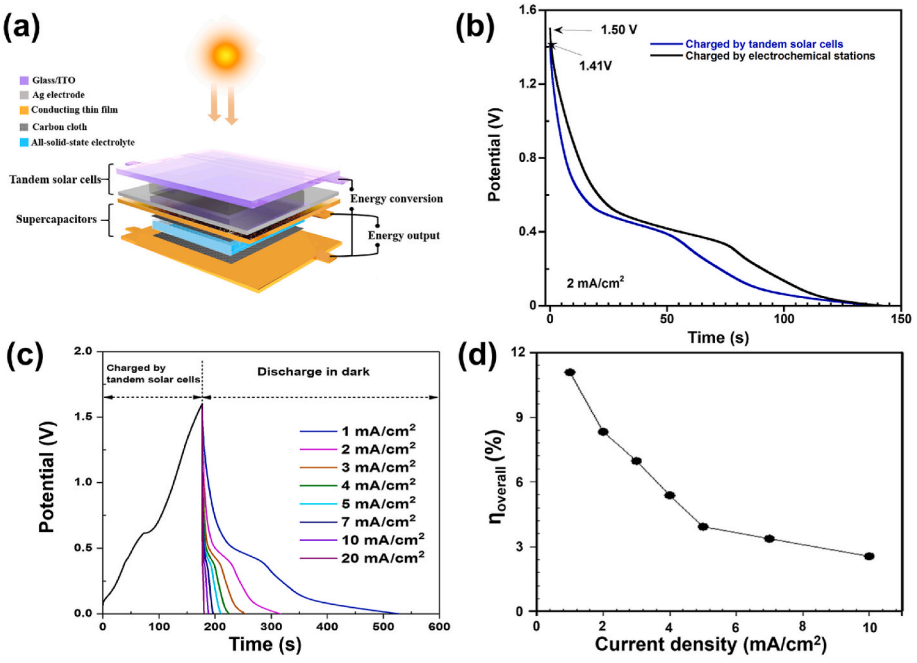

Fig. 4. (a) Device structure of the wireless portable light-weight self-charging power packs by tandem solar cells integrated with the solid-state asymmetric supercapacitors (ASCs), (b) the discharge curves of the solid-state ASCs charged by either tandem solar cells or an electrochemical station, (c) the GCD curves of the wireless portable light-weight self-charging power packs charged by tandem solar cells and then discharged in dark at different current densities, and (d) the overall efficiencies of the wireless portable light-weight self-charging power packs operated at different discharge current densities.

the work reported in this paper.

Acknowledgments

The authors acknowledge the National Science Foundation (ECCS/EPMD1903303) and Air Force Office of Scientific Research (AFOSR) (through the Organic Materials Chemistry Program, Grant Number: FA9550-15-1-0292, Program Manager, Dr. Kenneth Caster) for financial supports.

Appendix A. Supplementary data

Supplementary data to this article can be found online at https://doi.org/10.1016/j.nanoen.2020.105397.

References

[1] Z. Wen, M.-H. Yeh, H. Guo, J. Wang, Y. Zi, W. Xu, J. Deng, L. Zhu, X. Wang, C. Hu, Sci. Adv. 2 (2016), e1600097, https://doi.org/10.1126/sciadv.1600097.
[2] W. Deng, T. Yang, L. Jin, C. Yan, H. Huang, X. Chu, Z. Wang, D. Xiong, G. Tian, Y. Gao, Nanomater. Energy 55 (2019) 516–525, https://doi.org/10.1016/j.nanoen.2018.10.049.
[3] L. Li, Z. Lou, D. Chen, K. Jiang, W. Han, G. Shen, Small 14 (2018) 1702829, https://doi.org/10.1002/smll.201702829.
[4] Q. Zhang, Z. Zhang, Q. Liang, F. Gao, F. Yi, M. Ma, Q. Liao, Z. Kang, Y. Zhang, Nanomater. Energy 55 (2019) 151–163, https://doi.org/10.1016/j.nanoen.2018.10.078.
[5] M.A. Pellitero, A. Guimerà, M. Kitsara, R. Villa, C. Rubio, B. Lakard, M.-L. Doche, J.-Y. Hihn, F.J. Del Campo, Chem. Sci. 8 (2017) 1995–2002, https://doi.org/10.1039/C6SC04469G.
[6] F. Wu, P. Yu, L. Mao, Chem. Soc. Rev. 46 (2017) 2692–2704, https://doi.org/10.1039/C7CS00148G.
[7] P. Dong, M.-T.F. Rodrigues, J. Zhang, R.S. Borges, K. Kalaga, A.L. Reddy, G. G. Silva, P.M. Ajayan, J. Lou, Nanomater. Energy 42 (2017) 181–186, https://doi.org/10.1016/j.nanoen.2017.10.035.
[8] P. Du, X. Hu, C. Yi, H.C. Liu, P. Liu, H.L. Zhang, X. Gong, Adv. Funct. Mater. 25 (2015) 2420–2427, https://doi.org/10.1002/adfm.201500335.
[9] Z. Zhang, X. Chen, P. Chen, G. Guan, L. Qiu, H. Lin, Z. Yang, W. Bai, Y. Luo, H. Peng, Adv. Mater. 26 (2014) 466–470, https://doi.org/10.1002/adma.201302951.
[10] X. Xu, S. Li, H. Zhang, Y. Shen, S.M. Zakeeruddin, M. Graetzel, Y.-B. Cheng, M. Wang, ACS Nano 9 (2015) 1782–1787, https://doi.org/10.1021/nn506651m.
[11] W. Li, J. Zheng, B. Hu, H.-C. Fu, M. Hu, A. Veyssal, Y. Zhao, J.-H. He, T.L. Liu, A. Ho-Baillie, Nat. Mater. (2020) 1–6, https://doi.org/10.1038/s41563-020-0720-x.
[12] Q. Liu, Y. Jiang, K. Jin, J. Qin, J. Xu, W. Li, J. Xiong, J. Liu, Z. Xiao, K. Sun, S. Yang, X. Zhang, L. Ding, Sci. Bull. 65 (2020) 272–275, https://doi.org/10.1016/j.scib.2020.01.001.
[13] Nrel Efficiency Chart. https://www.nrel.gov/pv/assets/pdfs/best-reserch-cell-efficiencies.20190802.pdf, 2019 accessed: August 2019.
[14] G. Wang, F.S. Melkonyan, A. Facchetti, T.J. Marks, Angew. Chem. Int. Ed. 58 (2019) 4129–4142, https://doi.org/10.1002/anie.201808976.
[15] K. Wang, L. Zheng, T. Zhu, X. Yao, C. Yi, X. Zhang, Y. Cao, L. Liu, W. Hu, X. Gong, Nanomater. Energy 61 (2019) 352–360, https://doi.org/10.1016/j.nanoen.2019.04.073.
[16] D. Shi, V. Adinolfi, R. Comin, M. Yuan, E. Alarousu, A. Buin, Y. Chen, S. Hoogland, A. Rothenberger, K. Katsiev, Science 347 (2015) 519–522, https://doi.org/10.1126/science.aaa2725.
[17] L. Meng, Y. Zhang, X. Wan, C. Li, X. Zhang, Y. Wang, X. Ke, Z. Xiao, L. Ding, R. Xia, Science 361 (2018) 1094–1098, https://doi.org/10.1126/science.aat2612.
[18] A.F. Palmstrom, G.E. Eperon, T. Leijtens, R. Prasanna, S.N. Habisreutinger, W. Nemeth, E.A. Gaulding, S.P. Dunfield, M. Reese, S. Nanayakkara, Joule 3 (2019) 2193–2204, https://doi.org/10.1016/j.joule.2019.05.009.
[19] S. Albrecht, M. Saliba, J.P.C. Baena, F. Lang, L. Kegelmann, M. Mews, L. Steier, A. Abate, J. Rappich, L. Korte, Energy Environ. Sci. 9 (2016) 81–88, https://doi.org/10.1039/C5EE02965A.
[20] Q. Han, Y.-T. Hsieh, L. Meng, J.-L. Wu, P. Sun, E.-P. Yao, S.-Y. Chang, S.-H. Bae, T. Kato, V. Bermudez, Science 361 (2018) 904–908, https://doi.org/10.1126/science.aat5055.
[21] H. Shen, J. Peng, D. Jacobs, N. Wu, J. Gong, Y. Wu, S.K. Karuturi, X. Fu, K. Weber, X. Xiao, Energy Environ. Sci. 11 (2018) 394–406, https://doi.org/10.1039/C7EE02627G.
[22] J. Werner, C.-H. Weng, A. Walter, L. Fesquet, J.P. Seif, S. De Wolf, B. Niesen, C. Ballif, J. Phys. Chem. 7 (2016) 161–166, https://doi.org/10.1021/acs.jpclett.5b02686.
[23] N. Choudhary, C. Li, J. Moore, N. Nagaiah, L. Zhai, Y. Jung, J. Thomas, Adv. Mater. 29 (2017) 1605336, https://doi.org/10.1002/adma.201605336.
[24] Y. Wang, Y. Song, Y. Xia, Chem. Soc. Rev. 45 (2016) 5925–5950, https://doi.org/10.1039/C5CS00580A.
[25] Z. Chen, Y. Yang, Z. Ma, T. Zhu, L. Liu, J. Zheng, X. Gong, Adv. Funct. Mater. 29 (2019) 1904182, https://doi.org/10.1002/adfm.201904182.
[26] D.P. Dubal, N.R. Chodankar, D.-H. Kim, P. Gomez-Romero, Chem. Soc. Rev. 47 (2018) 2065–2129, https://doi.org/10.1039/C7CS00505A.
[27] S.S. Lee, K.H. Choi, S.H. Kim, S.Y. Lee, Adv. Funct. Mater. 28 (2018) 1705571, https://doi.org/10.1002/adfm.201705571.
[28] G. Wang, L. Zhang, J. Zhang, Chem. Soc. Rev. 41 (2012) 797–828, https://doi.org/10.1039/C1CS15060J.
[29] A. Sumboja, J. Liu, W.G. Zheng, Y. Zong, H. Zhang, Z. Liu, Chem. Soc. Rev. 47 (2018) 5919–5945, https://doi.org/10.1039/C8CS00237A.
[30] F. Wang, X. Wu, X. Yuan, Z. Liu, Y. Zhang, L. Fu, Y. Zhu, Q. Zhou, Y. Wu, W. Huang, Chem. Soc. Rev. 46 (2017) 6816–6854, https://doi.org/10.1039/C7CS00205J.
[31] T. Lu, S. Dong, C. Zhang, L. Zhang, G. Cui, Coord. Chem. Rev. 332 (2017) 75–99, https://doi.org/10.1016/j.ccr.2016.11.005.
[32] A. Banerjee, S. Bhatnagar, K.K. Upadhyay, P. Yadav, S. Ogale, ACS Appl. Mater. Interfaces 6 (2014) 18844–18852, https://doi.org/10.1021/am504333z.
[33] P. Yang, Z. Wu, Y. Jiang, Z. Pan, W. Tian, L. Jiang, L. Hu, Adv. Energy Mater. 8 (2018) 1801392, https://doi.org/10.1002/aenm.201801392.
[34] C. Xiong, M. Li, S. Nie, W. Dang, W. Zhao, L. Dai, Y. Ni, J. Power Sources 471 (2020) 228448, https://doi.org/10.1016/j.jpowsour.2020.228448.
[35] P. Flouda, A.H. Quinn, A.G. Patel, D. Loufakis, D.C. Lagoudas, J.L. Lutkenhaus, Nanoscale 12 (2020) 16840–16850, https://doi.org/10.1039/D0NR04573J.
[36] J. Ju, J. Ma, Y. Wang, Y. Cui, P. Han, G. Cui, Energy Storage Mater. 20 (2019) 269–290, https://doi.org/10.1016/j.ensm.2018.11.025.
[37] S. Zhai, L. Wei, H.E. Karahan, X. Chen, C. Wang, X. Zhang, J. Chen, X. Wang, Y. Chen, Energy Storage Mater. 19 (2019) 102–123, https://doi.org/10.1016/j.ensm.2019.02.020.
[38] C.J. Zhang, V. Nicolosi, Energy Storage Mater. 16 (2019) 102–125, https://doi.org/10.1016/j.ensm.2018.05.003.
[39] Z. Xiao, X. Jia, D. Li, S. Wang, X. Geng, F. Liu, J. Chen, S. Yang, T.P. Russell, L. Ding, Sci. Bull. 62 (2017) 1494–1496, https://doi.org/10.1016/j.scib.2017.10.017.
[40] X. Hu, C. Yi, M. Wang, C.H. Hsu, S. Liu, K. Zhang, C. Zhong, F. Huang, X. Gong, Y. Cao, Adv. Energy Mater. 4 (2014) 1400378, https://doi.org/10.1002/aenm.201400378.
[41] T. Yang, D. Qin, L. Lan, W. Huang, X. Gong, J. Peng, Y. Cao, Sci. China Chem. 55 (2012) 755–759, https://doi.org/10.1007/s11426-012-4512-2.
[42] C. Zuo, L. Ding, Adv. Energy Mater. 7 (2017) 1601193, https://doi.org/10.1002/aenm.201601193.
[43] X. Huang, K. Wang, C. Yi, T. Meng, X. Gong, Adv. Energy Mater. 6 (2016) 1501773, https://doi.org/10.1002/aenm.201501773.
[44] W. Xu, L. Zheng, X. Zhang, Y. Cao, T. Meng, D. Wu, L. Liu, W. Hu, X. Gong, Adv. Energy Mater. 8 (2018) 1703178, https://doi.org/10.1002/aenm.201703178.
[45] T. Zhu, Y. Yang, L. Zheng, L. Liu, M.L. Becker, X. Gong, Adv. Funct. Mater. 30 (2020) 1909487, https://doi.org/10.1002/adfm.201909487.
[46] T. Zhu, Y. Yang, X. Yao, Z. Huang, L. Liu, W. Hu, X. Gong, ACS Appl. Mater. Interfaces 12 (2020) 15456–15463, https://doi.org/10.1021/acsami.9b22891.
[47] C. Liu, C. Yi, K. Wang, Y. Yang, R.S. Bhatta, M. Tsige, S. Xiao, X. Gong, ACS Appl. Mater. Interfaces 7 (2015) 4928–4935, https://doi.org/10.1021/am509047g.
[48] T. Zhu, L. Zheng, Z. Xiao, X. Meng, L. Liu, L. Ding, X. Gong, Solar RRL 3 (2019) 1900322, https://doi.org/10.1002/solr.201900322.
[49] C. Lee, S. Lee, G.-U. Kim, W. Lee, B.J. Kim, Chem. Rev. 119 (2019) 8028–8086, https://doi.org/10.1021/acs.chemrev.9b00044.
[50] F. Yang, P. Zhang, M.A. Kamarudin, G. Kapil, T. Ma, S.J. Hayase, Adv. Funct. Mater. 28 (2018) 1804856, https://doi.org/10.1002/adfm.201804856.
[51] H. Lei, G. Yang, X. Zheng, Z.G. Zhang, C. Chen, J. Ma, Y. Guo, Z. Chen, P. Qin, Y. Li, Solar RRL 1 (2017) 1700038, https://doi.org/10.1002/solr.201700038.
[52] C.-C. Chen, S.-H. Bae, W.-H. Chang, Z. Hong, G. Li, Q. Chen, H. Zhou, Y. Yang, Mater. Horiz. 2 (2015) 203–211, https://doi.org/10.1039/C4MH00237G.
[53] J. Liu, S. Lu, L. Zhu, X. Li, W.C. Choy, Nanoscale 8 (2016) 3638–3646, https://doi.org/10.1039/C5NR07457F.
[54] Y. Liu, L.A. Renna, M. Bag, Z.A. Page, P. Kim, J. Choi, T. Emrick, D. Venkataraman, T.P. Russell, ACS Appl. Mater. Interfaces 8 (2016) 7070–7076, https://doi.org/10.1021/acsami.5b12740.
[55] J. Seifter, Y. Sun, A.J. Heeger, Adv. Mater. 26 (2014) 2486–2493, https://doi.org/10.1002/adma.201305160.
[56] K. Wang, L. Zheng, T. Zhu, L. Liu, M.L. Becker, X. Gong, Nanomater. Energy 67 (2020) 104229, https://doi.org/10.1016/j.nanoen.2019.104229.
[57] S.R. Cowan, N. Banerji, W.L. Leong, A.J. Heeger, Adv. Funct. Mater. 22 (2012) 1116–1128, https://doi.org/10.1002/adfm.201101632.
[58] S.R. Cowan, A. Roy, A.J. Heeger, Phys. Rev. B 82 (2010) 245207, https://doi.org/10.1103/PhysRevB.82.245207.
[59] M.D. Stoller, S. Park, Y. Zhu, J. An, R.S. Ruoff, Nano Lett. 8 (2008) 3498–3502, https://doi.org/10.1021/nl802558y.
[60] Y. Zhang, Z. Hu, Y. Liang, Y. Yang, N. An, Z. Li, H. Wu, J. Mater. Chem. 3 (2015) 15057–15067, https://doi.org/10.1039/C5TA02479J.
[61] Z. Chen, L. Zheng, T. Zhu, Z. Ma, Y. Yang, C. Wei, L. Liu, X. Gong, Adv. Electron. Mater. 5 (2019) 1800721, https://doi.org/10.1002/aelm.201800721.
[62] B. Balamuralitharan, S. Karthick, S.K. Balasingam, K. Hemalatha, S. Selvam, J. A. Raj, K. Prabakar, Y. Jun, H.J. Kim, Energy Technol. 5 (2017) 1953–1962, https://doi.org/10.1002/ente.201700097.
[63] H.-P. Cong, X.-C. Ren, P. Wang, S.-H. Yu, Energy Environ. Sci. 6 (2013) 1185–1191, https://doi.org/10.1039/C2EE24203F.
[64] K. Ghosh, C.Y. Yue, M.M. Sk, R.K. Jena, ACS Appl. Mater. Interfaces 9 (2017) 15350–15363, https://doi.org/10.1021/acsami.6b16406.
[65] H. Yuan, F. Ma, X. Wei, J.L. Lan, Y. Liu, Y. Yu, X. Yang, H.S. Park, Adv. Energy Mater. (2020) 2001418, https://doi.org/10.1002/aenm.202001418.

[66] V. Augustyn, P. Simon, B. Dunn, Energy Environ. Sci. 7 (2014) 1597–1614, https://doi.org/10.1039/C3EE44164D.
[67] Q. Jiang, N. Kurra, C. Xia, H.N. Alshareef, Adv. Energy Mater. 7 (2017) 1601257, https://doi.org/10.1002/aenm.201601257.
[68] W. Xu, Z. Jiang, Q. Yang, W. Huo, M.S. Javed, Y. Li, L. Huang, X. Gu, C. Hu, Nanomater. Energy 43 (2018) 168–176, https://doi.org/10.1016/j.nanoen.2017.10.046.
[69] D. Liu, Q. Li, H. Zhao, J. Mater. Chem. 6 (2018) 11471–11478, https://doi.org/10.1039/C8TA02580K.
[70] W. Si, C. Yan, Y. Chen, S. Oswald, L. Han, O.G. Schmidt, Energy Environ. Sci. 6 (2013) 3218–3223, https://doi.org/10.1039/C3EE41286E.
[71] W. Li, F. Gao, X. Wang, N. Zhang, M. Ma, Angew. Chem. 128 (2016) 9342–9347, https://doi.org/10.1002/ange.201603417.
[72] S. Zhu, L. Li, J. Liu, H. Wang, T. Wang, Y. Zhang, L. Zhang, R.S. Ruoff, F. Dong, ACS Nano 12 (2018) 1033–1042, https://doi.org/10.1021/acsnano.7b03431.
[73] Y. Zhang, B. Wang, F. Liu, J. Cheng, X.-w. Zhang, L. Zhang, Nanomater. Energy 27 (2016) 627–637, https://doi.org/10.1016/j.nanoen.2016.08.013.
[74] R. Liu, J. Wang, T. Sun, M. Wang, C. Wu, H. Zou, T. Song, X. Zhang, S.-T. Lee, Z. L. Wang, Nano Lett. 17 (2017) 4240–4247, https://doi.org/10.1021/acs.nanolett.7b01154.
[75] W. Li, H.C. Fu, L. Li, M. Cabán-Acevedo, J.H. He, S. Jin, Angew. Chem. 128 (2016) 13298–13302, https://doi.org/10.1002/ange.201606986.
[76] X. Yun, Z. Xiong, L. Tu, L. Bai, X. Wang, Carbon 125 (2017) 308–317, https://doi.org/10.1016/j.carbon.2017.09.063.
[77] K. Siuzdak, R. Bogdanowicz, M. Sawczak, M. Sobaszek, Nanoscale 7 (2015) 551–558, https://doi.org/10.1039/C4NR04417G.